WILEY | Hindawi

Research Article

Accuracy of Distributed Strain Sensing with Single-Mode Fibre in Composite Laminates under Thermal and Vibration Loads

Yingwu Li [ID] and Zahra Sharif-Khodaei [ID]

Imperial College London, Exhibition Road, London SW7 2AZ, UK

Correspondence should be addressed to Yingwu Li; yingwu.li19@imperial.ac.uk

In this work, the strain measurement accuracy of single-mode fibre (SMF) under thermal and vibration loads is investigated by strain-frequency shift coefficient analyses. This research allows for the application of SMF sensors for structural health monitoring in real operational conditions. The strain measurement accuracy under combined static and thermal load is investigated experimentally, which demonstrated that temperature fluctuations induce non-negligible errors in the strain measurement, even with temperature compensation applied. The temperature fluctuation range which can induce measurement errors is quantified as less than $-20°C$ or higher than $55°C$. In addition, a fatigue experiment is conducted to investigate the measurement accuracy under low-frequency vibration load. The results of the fatigue experiment demonstrate that the vibrations mainly increase the ratio of null values in strain measurements. Findings from experiments can be applied to enhance structural health monitoring accuracy and reduce false positives. This study has important implications for the service application of distributed optical fibre sensing for composite structure health monitoring.

1. Introduction

Carbon fibre reinforced polymers (CFRPs) have been widely used in various aircraft structures [1, 2], due to their outstanding advantages including light weightedness, superior strength, and low costs. However, durability, unforeseen, and complex damage scenarios are challenges that require attention. Damage types in CFRP include delamination, debonding, fibre breakage, and matrix cracking and are difficult to characterize and detect [3, 4], which makes the monitoring of the integrity of composite parts particularly important. Strain measurement is an important method for structural health monitoring (SHM) because the strain distribution usually changes when damage is initiated in a structure [5, 6]. An ideal sensor for strain measurement in CFRP is the single-mode fibre (SMF) which is interrogated by an optical frequency domain reflectometry (OFDR) system [7]. This is because SMFs are light, cheap, easily available, and enable distributed strain sensing with high spatial accuracy.

Various fibre optical (FO) sensors have been adopted in different SHM applications [7–9]. For example, buckling detection based on distributed FO sensors [10], a hybrid piezoelectric-fibre optic system based on fibre Bragg gratings (FBG) [11, 12], embedded FBG sensors in SHM of complex composite structures [13], and sandwich panel [14]. In addition, FO sensors are adopted in composite manufacturing monitoring [15, 16] and damage detection [17, 18]. For in-field applications, however, many more FBG sensors are required than distributed FO sensors to obtain sufficient measurements, which results in higher system weight and cost.

In OFDR systems, Rayleigh backscattering of SMFs is used to interfere with the incident light to produce a beat signal. The frequency and amplitude of this beat signal correspond to a specific location on the SMF and the Rayleigh backscattering intensity at that location, respectively, since the light frequency of Rayleigh backscattering does not change during the previous processes. Moreover, the intensity of this backscattering is related to

defects introduced during the manufacturing process. The beat signal is adopted as a unique code to identify a position on the SMF [19]. When this position is subjected to an external load, the resulting strain causes a frequency shift of the beat signal which is then calculated by matching the beat signals before and after loading. The strain is finally measured using a determined strain-frequency shift coefficient. This coefficient is the ratio between strain shift and corresponding frequency shift.

SMFs interrogated by OFDR have been adopted as strain sensors in many studies for various analyses of composite structures [5]. For example, shape sensing of a beam-like composite structure [20], damage detection in composite wind turbines [21], multiparameter strain sensing of composites [22], hygrothermal degradation of single fibre composite [23], and health state assessment of composite laminates during manufacturing [24]. Furthermore, the small size of SMF makes it suitable for application to complex composite structures including cylinders [25], bonded lap joints [26], and CFRP plates with circular holes [27]. As the measurement results of SMFs are influenced by both mechanical and thermal loads, many studies have been conducted on temperature compensation to improve strain measurement accuracy [28]. However, the temperature compensation cannot eliminate the strain measurement error induced by strain transfer coefficient change due to temperature fluctuations [29]. In addition, the adhesion and embedding quality of SMF is also proved to be affected by mechanical loading [30, 31]. Factors including temperature fluctuations and mechanical vibrations are inevitable in field applications, which induce nonnegligible errors in strain measurement even with temperature compensation applied. Therefore, the investigation of strain measurement accuracy under thermal and vibration loads is essential for the field applications of SMF-based distributed sensing in CFRP.

Several researchers have validated the FO sensors for strain measurement under quasistatic loading [26, 28, 32]. However, the operational conditions of aircraft results in low-frequency vibration in-service in which the SMF sensors will also be exposed to. Therefore, the accuracy of distributed strain sensing under vibration load needs to be demonstrated. When calculating the strain based on distributed SMFs, the strain-frequency shift coefficient is usually obtained in a straightforward way by reading the frequency shift under a known load [33–36]. This method is unable to obtain high-precision strain information in a complex environment such as during flight. To address this problem, this paper has studied the strain measurement accuracy of distributed SMF under thermal and vibration loads for the first time. The results show that environmental condition is one of the critical factors that need to be considered for higher accuracy of strain sensing with distributed SMFs. It also demonstrates that at a certain temperature range, the strain-frequency shift coefficient can be considered constant, but outside its range, it needs to be compensated for. The results of this work can be used as important references to service applications using distributed SMFs in composite structure health monitoring.

In this paper, the measurement error of SMF under thermal and vibration loads is investigated by strain-frequency shift coefficient analyses. The SMF and strain gauges are surface mounted on a composite laminate coupon. The strain gauge measurements are used as the reference strain. The fluctuation of the strain-frequency shift coefficient under thermal load is investigated by a static loading experiment first, followed by a fatigue experiment to investigate the fluctuation of this coefficient under low-frequency vibration load. The influence of temperature and vibration loads on the frequency shift is studied in combination and separately to isolate their effect on the strain measurement accuracy.

2. Experimental Setup

2.1. Specimen and Sensors. The size of the specimen manufactured and tested is $50 \times 100 \times 3.2$ mm. This specimen is made of CYTEC noncrimp fabric. The layout of this specimen is $[45/90/-45/0/45/0_2/-45]_s$. The thickness is 3.2 mm. The elastic properties of the lamina used in this paper are shown in Table 1.

The single mode fibre (SM1500 (9/125)P manufactured by FIBERCORE) and strain gauges are both adopted in the experiment for strain measurement. The SM1500 (9/125)P with polyimide coating has a variety of features such as high-temperature survival, bend insensitivity, and enhanced photosensitivity, which makes it very attractive for distributed strain sensing. In this work, the single mode fibres were adopted for strain measurement of composite laminates under both mechanical load (static and low-frequency dynamic load) and thermal load. The frequency shift of SMF can be related to a temperature or strain change. This relationship is expressed in equation as follows:

$$\Delta v = K_T \Delta T + K_\varepsilon \Delta \varepsilon, \tag{1}$$

where Δv is the frequency shift; ΔT and $\Delta \varepsilon$ are temperature and strain changes, respectively; K_T express the temperature-frequency shift coefficient (or known as conversion factors from frequency shift to temperature change); K_ε is the strain-frequency shift coefficient (or known as conversion factors from frequency shift to strain). The detailed expressions of these two coefficients are reported in the study [37]. Both K_T and K_ε are usually regarded as constant in the reported applications. For example, this equation works in a temperature range of −40°C to 220°C or in a strain range of $−10000 \, \mu\varepsilon–10000 \, \mu\varepsilon$ for the ODiSI-B system manufactured by LUNA Ltd. However, the experiment results in this paper demonstrate that K_ε is not a constant under different ambient temperatures, which may induce strain measurement errors in real operational applications.

The SMF and strain gauges are bonded to the surface of the specimen by a thermoplastic adhesive film based on modified polyolefins (Pontacol 22.100). This type of thermoplastic adhesive film is adopted because of advantages including easy maintenance, high peel strength, and controllable thickness [17, 38–40]. As shown in Figure 1, two "S" shape SMF, called SMF1 and SMF2, are mounted on each

TABLE 1: Elastic parameters of the lamina used in this paper.

Parameters	Symbol	Unit	Value
Elastic modulus	E_{11}	MPa	111800
	$E_{22} = E_{33}$	MPa	7620
Poisson's ratio	v_{23}	—	0.450
	$v_{12} = v_{13}$	—	0.290
Shear modulus	G_{23}	MPa	2628
	$G_{12} = G_{13}$	MPa	4130

side of the specimen independently, to provide strain readings in different directions. A strain gauge is mounted on each side of the specimen: on side 1 at $-45°$ with respect to the fibre direction, defined as Gauge1 (as shown in Figure 1(a)), and at $0°$ on side 2 (as shown in Figure 1(b)) defined at Gauge2. The data acquired by these two strain gauges are used as a reference strain for the strain-frequency shift coefficient calculation.

2.2. Static Loading Experiment. In the static loading experiment, a simultaneous loading of temperature and tension was applied to the specimen. This load was realized by the combination of an Instron dual-column machine (Instron 50 kN 5960 system) and a fitted environmental chamber (Instron 3119–600) shown in Figure 2(a). Figures 2(b) and 2(c) show sides 1 and 2 of the specimen in the test setup. The SMF data were acquired by the ODiSI-B system manufactured by LUNA Ltd.

Two types of tests were carried out as follows: the first test scenario is a measurement of frequency shift with a tension load, under different temperatures. In this test, the temperature changed from $-30°$C to $80°$C in steps of $5°$C. Each time when the temperature stabilised, the reference spectrum of the SMF sensor was reset. A 0 to 10 kN (625 MPa) tensile load was then applied to the specimen, and the frequency shift of SMF was acquired. Therefore, this frequency shift is only caused by tension load under different temperatures. Another test scenario was to continuously measure the frequency change with tension and temperature variation. In this test, the temperature changed from $-30°$C to $80°$C in steps of $5°$C. The reference spectrum of SMF is only set once at $-30°$C. A 0 to 10 kN (625 MPa) tension load is directly applied to the specimen each time after the temperature became stable. Therefore, the measured frequency shift in this test scenario contains the combined effects of both tension and temperature variation.

2.3. Fatigue Experiment. In the fatigue experiment, a 5 Hz sine wave signal was used as a vibration load. The range of this load was set between 0 and 3 kN (187.5 MPa). This vibration load was realized by an Instron 8032 servo-hydraulic universal testing machine. The fatigue experiment lasted for a whole week to reach more than 1.6 million fatigue cycles. This experiment was carried out at room temperature. The strain gauge data were measured automatically every 1000 fatigue cycles. As for the SMF data, only SMF2 was measured manually about every hour during the day. This is because the ODiSI-B system cannot support

multiple channels during dynamic measurements. The main purpose of the fatigue experiment is the applicability of the SMF under continuous dynamic measurement and frequency-strain coefficient stability under low frequency vibration load.

3. Data Analyses of Static Loading Experiment

3.1. Data Cleaning and Reconstruction. In the static loading experiment, many outliers and null values are observed in the measurement data acquired by the ODiSI-B system because of the similarity degenerate between measurement and reference Rayleigh backscattering under high load, which can significantly affect the results [41, 42]. Therefore, an algorithm is developed for data cleaning and reconstruction. The data of SMF2 at $-30°$C in an independent test are used to illustrate the data reconstruction algorithm. The first step is outlier elimination. This is realized by the local outlier factor (LOF) algorithm [43]. This method is adopted because of the continuity of strain measurements. A constant LOF (Δv_{LOF} in equation (2)) is sufficient to achieve the outlier elimination in this experiment since the outliers are orders of magnitude greater than other data points. Assuming that the measurements of SMF are $(x_i, \Delta v_i)$, $(i = 1, 2, \ldots, N)$, the data after the elimination with the LOF algorithm ($\Delta \widetilde{v}_i$) is shown in equation as follows:

$$\Delta \widetilde{v}_i = \begin{cases} \text{null}, & \Delta v_i' \geq \Delta v_{LOF}, \\ \Delta v_i, & \Delta v_i' < \Delta v_{LOF}, \end{cases} \quad i = 1, 2, 3, \ldots, N. \quad (2)$$

After the elimination, the data of the surface-mounted area is extracted according to peak alignment. Since the spatial resolution of the ODiSI-B system is 2.6 mm, 73 sensing segments are included along the fibre length according to its layout. The peak value of measurement data indicates the sensing segment along the loading direction in the static loading experiment (around the 25th and 49th sensing segment as shown in Figure 3(a)). Therefore, the data along the fibre orientation are extracted according to the locations of the peak values. The data after filtering and extraction are shown in Figure 3(b). The x-axis shows the spatial distribution of the measurement segments of SMF, which range from 0 to 0.2 m; the y-axis shows the static load from 0 to 10 kN; the z-axis plots the frequency shift of ODiSI-B at each measurement segment under each static load.

Null values are observed after outlier elimination, which implies a significant information loss. Temporal-based and spatial-based reconstruction methods [44] are adopted to address this problem since the measurement data have a clear spatial and temporal pattern. In the time domain, the linear fit between load and frequency shift is adopted first for data reconstruction. This is because of the linear relationship between the tension load and the measurements for every measurement segment on SMF. All missing data were reconstructed after the linear fit in the time domain. The results are shown in Figure 4(a). However, because of the low signal-noise ratio and measurement errors, there still exist
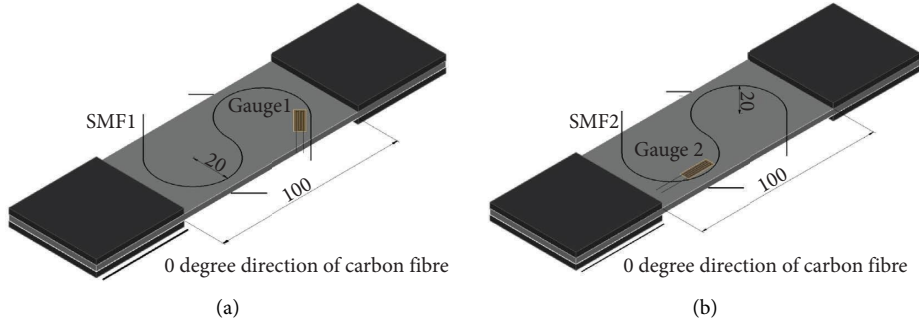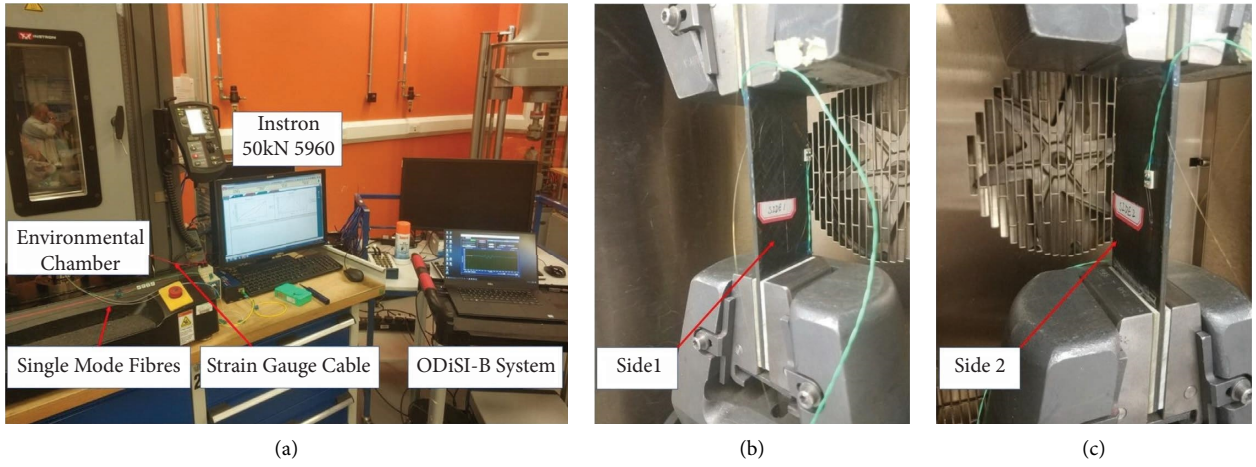
FIGURE 1: Layout of sensors on the specimen.

FIGURE 2: Static loading experiment setup.

errors after the linear fit. These errors (discontinuous value) are clearly indicated in Figure 4(a). Therefore, the robust locally weighted scatter-plot smoothing (RLOWESS) algorithm is adopted to eliminate these errors and to smooth the data in the temporal and spatial domain. The discrete measurements of SMF measurements after outlier elimination and linear fit reconstruction are $(x_i, \Delta\hat{v}_i), i = 1, 2, 3, \ldots, N$. The measurements within a local sliding window at $[x_p, x_q], (1 \leq p < q \leq N)$ are adopted for the RLOWESS algorithm. The weighted function adopted in this method is given by the symmetric tricube function shown as follows:

$$w_k = \left(1 - \left| \frac{x_{\lfloor (p+q)/2 \rfloor} - x_k}{d_{pq}} \right|^3 \right)^3 k = p, p+1, \ldots, q-1, q,$$

(3)

where w_k is the weight of the $k-th$ measurement in the linear regression; $x_{\lfloor (p+q)/2 \rfloor}$ is the centre of the local sliding window, which has the highest weight in linear regression; x_k is the measurements within the local sliding window; d_{pq} is the Euclidean length of the local sliding window. Therefore, the sum of the residual squares after weighted linear regression is expressed by equation as follows:

$$J(a, b) = \frac{1}{(q-p+1)} \sum_{k=p}^{q} w_k \left(a \cdot x_k + b - \Delta\hat{v}_k \right)^2 k$$

$$= p, p+1, \ldots, q-1, q,$$

(4)

where a and b are the estimated coefficients of weighted linear regression. Therefore, the optimal solution of a and b is obtained by minimising $J(a, b)$, as expressed in equation as follows:
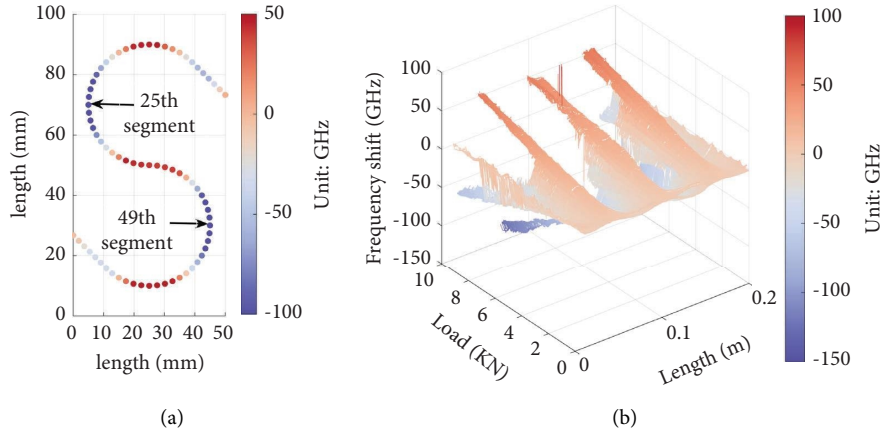
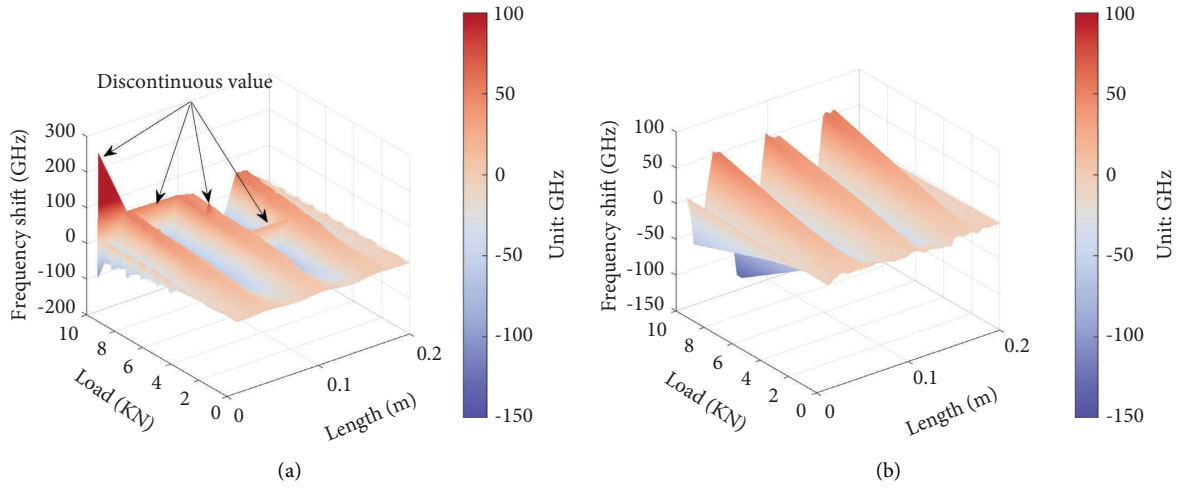FIGURE 3: Sensing segment distribution and measurement data of SMF2 in static loading experiment.

FIGURE 4: Data cleaning and reconstruction results of SMF2 measurements in static loading experiment.

$$\begin{cases} \dfrac{\partial J(a,b)}{\partial a} = \dfrac{2}{(q-p+1)} \sum_{k=p}^{q} w_k \cdot x_k \left(a \cdot x_k + b - \Delta \widehat{v}_k \right) = 0, \\[4mm] \dfrac{\partial J(a,b)}{\partial b} = \dfrac{2}{(q-p+1)} \sum_{k=p}^{q} w_k \left(a \cdot x_k + b - \Delta \widehat{v}_k \right) = 0, \end{cases} \qquad k = p, p+1, \ldots, q-1, q. \tag{5}$$

Following by the weighted linear regression mentioned previously, a modified weighted function based on regression residual is adopted to enhance the robustness of this algorithm. This modified weighted function is shown in equation as follows:

$$\widetilde{w}_k = \begin{cases} \left(1 - \left(\dfrac{r_k}{6\mathrm{Med}}\right)^2\right)^2, & r_k < 6\mathrm{Med}, \\[4mm] 0, & r_k \geq 6\mathrm{Med}, \end{cases} \qquad k = p, p+1, \ldots, q-1, q, \tag{6}$$

where $r_k = a \cdot x_k + b - \Delta \widehat{v}_k$ expresses the regression residuals; Med = $|\mathrm{median}(r_k)|$ is the median absolute deviation of the residuals. The result after data cleaning and reconstruction is shown in Figure 4(b).

It is worth noting that the smoothing process mentioned previously is intended to restore the outliers and null values that are a result of systematic errors of ODiSI-B. However, this process may inadvertently mask crucial strain features in proximity to the damaged region, thereby negatively impacting certain applications such as damage detection.

3.2. Temperature Compensation. The data cleaning and reconstruction algorithm successfully restored the results in both test scenarios. As mentioned previously, the recorded data in both tests are different: the continuous measurements from the second test scenario contain tension and temperature information, whereas measurements from the first test scenario are mainly influenced by tension load. To illustrate the measurement consistency of both scenarios, temperature compensation is applied to the continuous measurement test based on the data recorded at the part of the SMF, which is only exposed to thermal load. The continuous measurements from the second test scenario are compensated and then compared with the measurements from the first test scenario. The comparison result under 80°C is shown in Figure 5, where Figure 5(a) shows the results of distributed measurements at a 6 kN (375 MPa) tension load. Figure 5(b) shows the frequency shift along the load direction, under different tension loads. Note that the data of the 49th segment on SMF2 (Figure 3(a)) are adopted in this figure. This comparison illustrates that the compensated results of both test scenarios are highly consistent. Therefore, the measurements from the first test scenario are regarded as continuous measurements with temperature compensation in the following analyses.

3.3. Strain Measurement Accuracy under Thermal Load. The measurements from the first test scenario after data cleaning and reconstruction are adopted in strain calculation based on the previous analyses. Since these measurements are in the form of frequency shift of the SMF, the selection of the strain-frequency shift coefficient directly influences the strain results. The constant strain-frequency shift coefficient is usually used under different measurement states in real applications. However, the question raises that whether variability in operational conditions will also influence this coefficient. In other words, if the strain-frequency shift is calculated at room temperature, e.g., 20°C, can this coefficient be used to convert the SFM readings recorded at a different temperature into strain? Therefore, in this work, the strain-frequency shift coefficient at different ambient temperatures is investigated in detail.

The strain-frequency shift coefficient is calculated based on measurements of SMF2 and Gauge2, with Gauge2 measurements being adopted as the reference strain. Therefore, the reliability of these strain gauge measurements at different temperatures is first investigated. Under the experimental conditions in this paper, this stability can be directly reflected by the variation in the strain-load coefficient of Gauge2. This strain-load coefficient is the ratio between the strain shift and the corresponding load shift. This coefficient should be stable because it is not expected to see any reduction in the CFRP modulus at −30°C to 80°C [45]. However, as shown in Figure 6(a), a significant decreasing trend is observed at temperatures greater than 45°C. This decrease is mainly caused by the deterioration of the thermoplastic adhesive film used for bonding the sensors.

To obtain a reliable reference strain, the average value of the strain-load coefficient at temperatures below 45°C is adopted to calibrate the measurement strain of Gauge2 above 45°C. With the calibrated reference strain and SMF2 measurements near Gauge2 (49th segment shown in Figure 3(a)), the strain-frequency shift coefficient is directly calculated and shown in Figure 6(b). This coefficient is stable when the temperature stays between −20°C and 55°C. However, when the temperature becomes higher than 55°C or lower than −20°C, a significant decrease is observed. This decrease induces non-negligible errors in SMF strain even with temperature compensation when a constant strain-frequency coefficient is adopted. This conclusion is demonstrated by Figure 7(a) which shows a comparison of Gauge2 reference strain and the calculated strain from the SMF2 at 50°C and 80°C when the strain-frequency shift coefficient at 20°C is adopted. Note that the data of the 49th segment on SMF2 (Figure 3(a)) are adopted in this figure. Based on this conclusion, a further analysis of SMF strain error is conducted. In this analysis, the frequency shift under the current state and the strain-frequency shift coefficient under the baseline state are adopted to calculate the SMF strain. The error between the calculated SMF strain and the reference strain is defined as e_{tt_0} as follows:

$$e_{tt_0} = \frac{g(t_0)\Delta f - S_{gt}}{S_{gt}} \times 100\%, \qquad (7)$$

where t is the temperature of the current state; t_0 is the temperature of the baseline state; Δf expresses the frequency shift of the SMF under the current state; $g(t_0)$ expresses the strain-frequency coefficient for the baseline state; S_{gt} denotes the reference strain under the current state. The errors for different current and baseline state combinations are shown in Figure 7(b). In this figure, the *x*-axis is the temperature of the current state (the frequency shift data of SMF2 are adopted under this temperature); the *y*-axis shows the temperature of the baseline state (the strain-frequency shift coefficient is adopted under this temperature); the *z*-axis express the percent error of the calculated strain compared with the reference strain. For comparison with the reference strain, only the data of the 49th segment on SMF2 (Figure 3(a)) are adopted in this figure. This figure illustrates that e_{tt_0} increases rapidly when the temperature of the current or the baseline state is below −20°C or above 55°C. This result suggests that a constant strain-frequency shift coefficient cannot be adopted for strain measurement at all temperature conditions. However, there exists a temperature insensitive area according to Figure 7(b). When the temperature of both current and baseline states are between −20°C and 55°C, e_{tt_0} is less than 2% and a constant strain-frequency shift coefficient can be adopted. Therefore, the calibration of the strain-frequency shift coefficient is only necessary when the measurement temperature is out of this range.

3.4. Numerical Verification. The SMF strain is calculated and analyzed in the previous sections. For example, the calculated strain along SMF2 under different loads at 20°C is
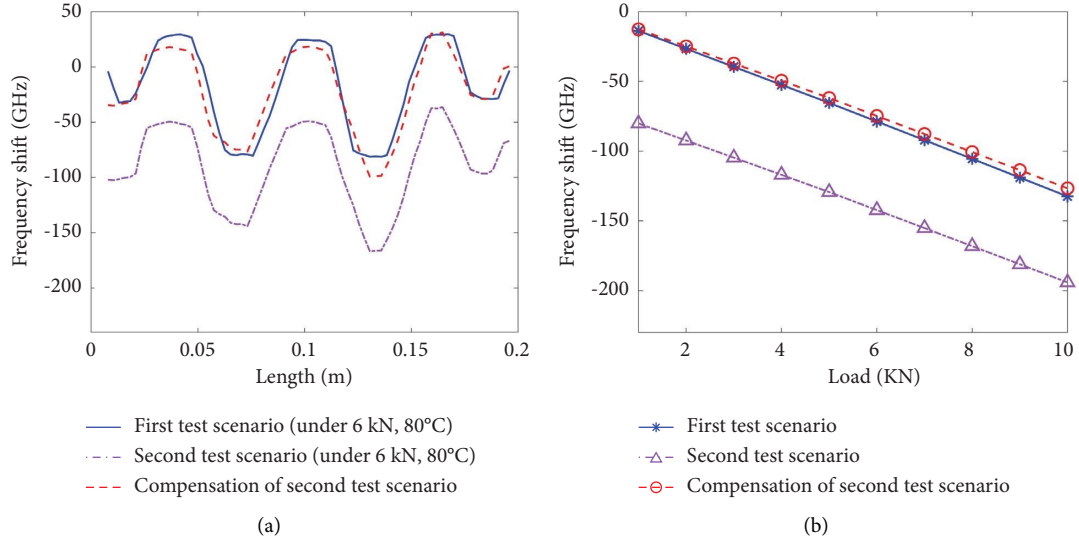
(a)

(b)

FIGURE 5: Temperature compensation results of SMF2 in static loading experiment.
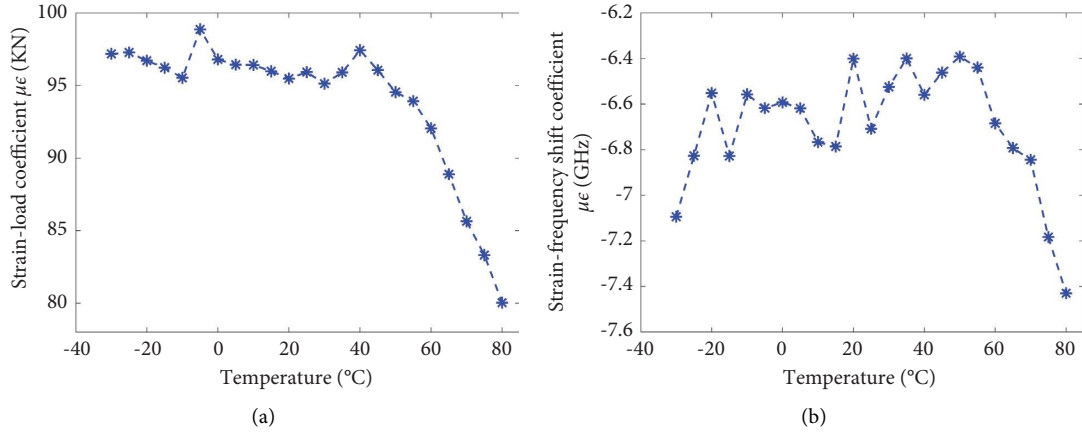

(a)

(b)

FIGURE 6: Strain-load coefficient of Gauge2 and strain-frequency shift coefficient of SMF2 under thermal load.

shown in Figure 8(a). To validate the reliability of the calculated strain, a numerical model is built based on the elastic parameters of the carbon fibre which is shown in Table 1. Figure 8(b) shows the model of the composite laminate. A 10 kN (625 MPa) tension load is applied to the short edge of the composite laminate. The simulation result is shown in Figure 8(c). The maximum displacement is 0.1145mm, which means that the strain of the specimen under 10 KN (625 MPa) tension is 1145$\mu\varepsilon$.

As shown in Figure 8(a), the calculated strain of SMF2 under 10 kN (625 MPa) tension at 0° direction is 943.7$\mu\varepsilon$ ($t_0 = t = 20$°C), which is less than the numerical result. This is mainly because of the strain transfer rate between the substrate and SMF. In the work of [46], a model is built to estimate this strain transfer rate α by equation (8). The expression of k in this equation is shown in equation (9) as follows:

$$\alpha = 1 - \frac{2 \sin h\left(0.5 k L_f\right)}{k L_f \cos h\left(kL\right)}, \tag{8}$$

$$\frac{1}{k^2} = \frac{E_f}{G_a}\left(\frac{r_f}{2} - \frac{\pi r_f^2}{D}\right)\left(\frac{h}{4} - \frac{r_f}{2}\right)$$
$$+ \frac{h_i}{2 G_m}\left[E_a\left(h - \frac{\pi r_f^2}{D}\right) - E_f \frac{\pi r_f^2}{D}\right], \tag{9}$$

where α is the strain transfer rate; L_f represents the sensing gauge length; r_f expresses the radius of SMF; h denotes bonding thickness; D is the bonding length; G_m is the shear modulus of composite laminate; E_f is the elastic modulus of SMF; h_i represents the influence depth of the shear stress; E_a denotes the elastic modulus of the adhesive film; G_a is the shear modulus of the adhesive film.
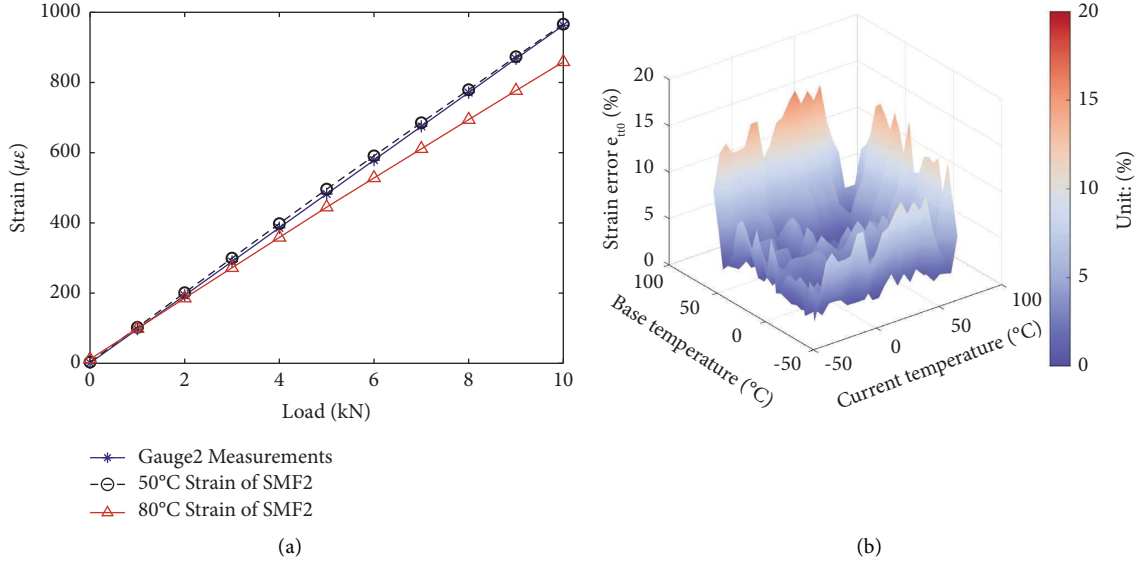
(a)

(b)

FIGURE 7: Strain calculation errors of SMF2 in static loading experiment.
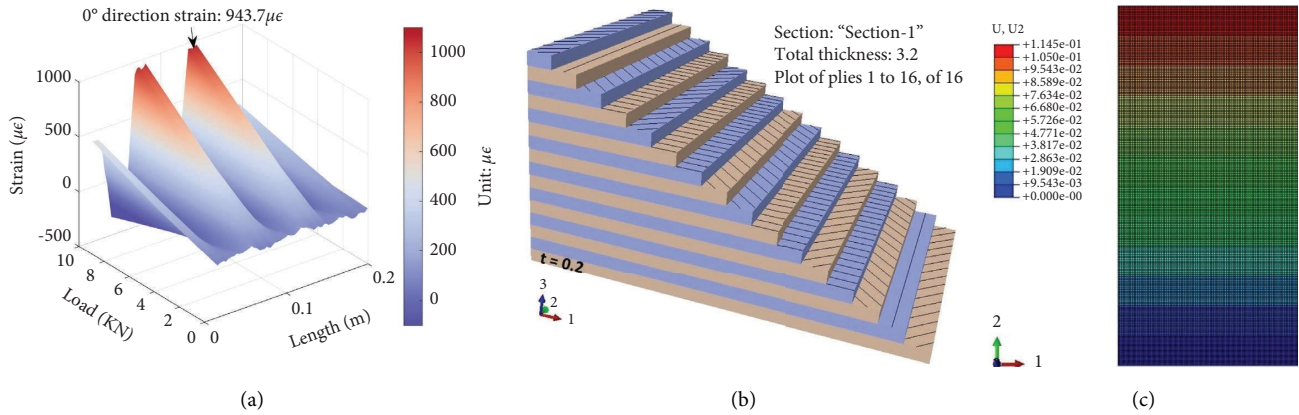

(a)

(b)

(c)

FIGURE 8: Strain measurements of SMF2 under 10 kN (625 MPa) tension and numerical modelling results.

TABLE 2: Parameters of thermoplastic adhesive film and SMF adopted in the experiment.

Parameters	Symbol	Unit	Value
Sensing gauge length	L_f	mm	10
SMF radius	r_f	mm	0.0625
Bonding thickness	h	mm	1
Influence depth	h_i	mm	1
Bonding width	D	mm	1
Bonding length	$2L$	mm	10
Shear modulus of composite laminate	$G_m \approx G_{23}$	MPa	2628
Elastic modulus of SMF	E_f	MPa	72000
Elastic modulus of film	E_a	MPa	2780
Shear modulus of film	G_a	MPa	1000

The parameters of the thermoplastic adhesive film and SMF adopted in this experiment are summarized in Table 2. With these parameters, the strain transfer rate is therefore obtained using equations (8) and (9), which was calculated to be 0.842 (set $G_m \approx G_{23}$). In this experiment, the strain transfer rate calculated from the modelling result and SMF measurement is 0.824. This result agrees fairly well with the value of the strain transfer rate calculated from the literature [46]. This result demonstrates that the calculated strain of SMF2 based on the proposed data cleaning and reconstruction, temperature compensation, and strain-frequency shift coefficient calibration is highly accurate and reliable.

4. Data Analyses of Fatigue Experiment

4.1. Dynamic Measurements and Data Resampling. In the fatigue experiment, the data of SMF2 and Gauge2 are measured under cyclic load with a frequency of 5 Hz and an amplitude of 3 kN (625 MPa). The SMF2 measurements at around 54000 cycles are shown in Figure 9(a). This diagram illustrates high-precision continuous sensing by the SMF under low-frequency vibration load. Figure 9(b) shows the strain data of Gauge2 at around 54000 cycles. As with the static measurements, SMF-based distributed sensing obtains more strain information on specimens than strain gauges.
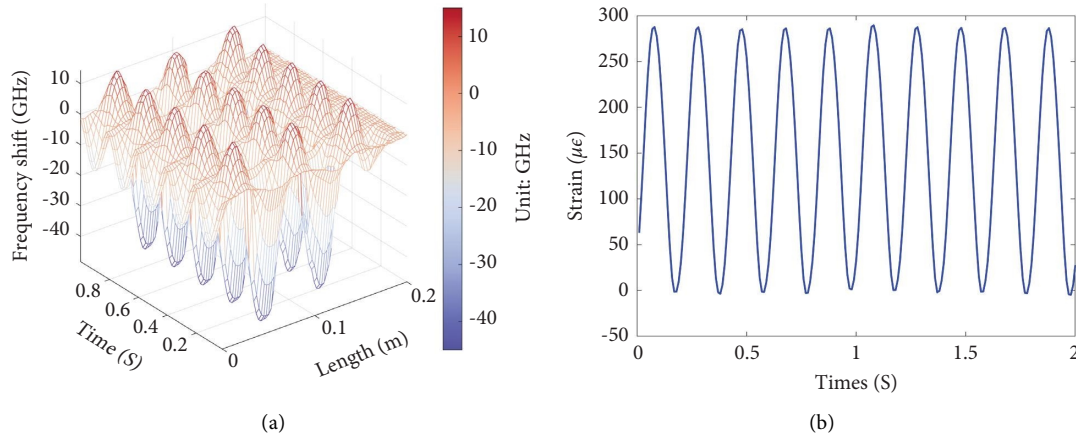
(a)

(b)

FIGURE 9: Measurements of SMF2 and Gauge2 in fatigue experiment (at around 54000 cycles).
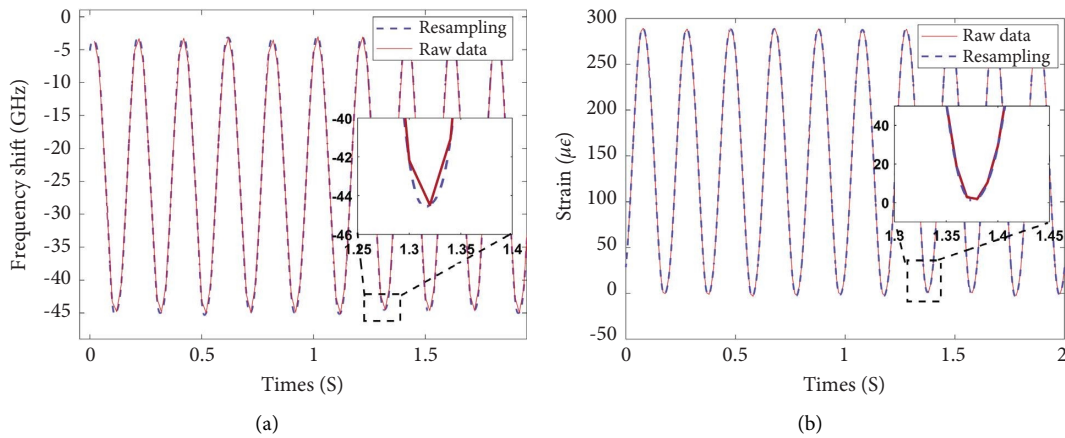

(a)

(b)

FIGURE 10: Data interpolation of single mode fibre and strain gauge measurements.

The sampling frequency of SMF2 and Gauge2 is 50 Hz and 100 Hz, respectively. To compare the measurement results of SMF2 and Gauge2, the SMF2 measurements near Gauge2 are adopted (49th segment shown in Figure 3(a)). An interpolation method is then adopted to unify the sampling frequency. The results of SMF2 and Gauge2 are shown in Figures 10(a) and 10(b), respectively. The sampling frequency after the interpolation is 5 kHz.

4.2. Strain Measurement Errors under Low Frequency Vibration Load. As with the static analysis, the Gauge2 measurements are adopted as the reference strain in the strain-frequency shift coefficient calculation of SMF2. Therefore, the reliability of Gauge2 measurements throughout the fatigue experiment is first investigated based on the analysis of the strain-load coefficient. The calculation result of this coefficient is shown in Figure 11(a). This figure illustrates that the ratio between the strain shift and the corresponding load shift is stable during the whole fatigue experiment. In addition, the value of this coefficient is consistent with the result in the static loading experiment as shown in Figure 6(a). However, the

reading of Gauge2 creeps with the increase of the fatigue cycle, even though the strain-load coefficient stays stable. This creep behaviour is illustrated in Figure 11(b) which shows the reading at 0 kN and 3 kN (187.5 MPa). In this figure, the reading of Gauge2 at 0 kN gradually creeps from $0\mu\varepsilon$ to $-100\mu\varepsilon$ throughout the whole fatigue experiment. Therefore, the Gauge2 reading at the beginning of the fatigue experiment was adopted as the reference strain during the whole fatigue experiment to avoid this creep effect.

The strain-frequency coefficient is then obtained based on the reference strain and reading of the 49th segment on SMF2 (Figure 3(a)) at 3 kN (187.5 MPa). The result of this coefficient is shown in Figure 12(a). The strain-frequency coefficient stays stable and is consistent with the result in the static loading experiment shown in Figure 6(b) during the whole fatigue experiment. Therefore, the strain under 0 to 3 kN (0 to 187.5 MPa) during the fatigue experiment measured by SMF2 is calculated based on the frequency shift of SMF2 and the strain-frequency coefficient. The peak values of the calculated strains are shown in Figure 12(b). A constant load is induced during the fatigue experiment because the reference spectrum of the SMF is set before the experiment, which is the reason for
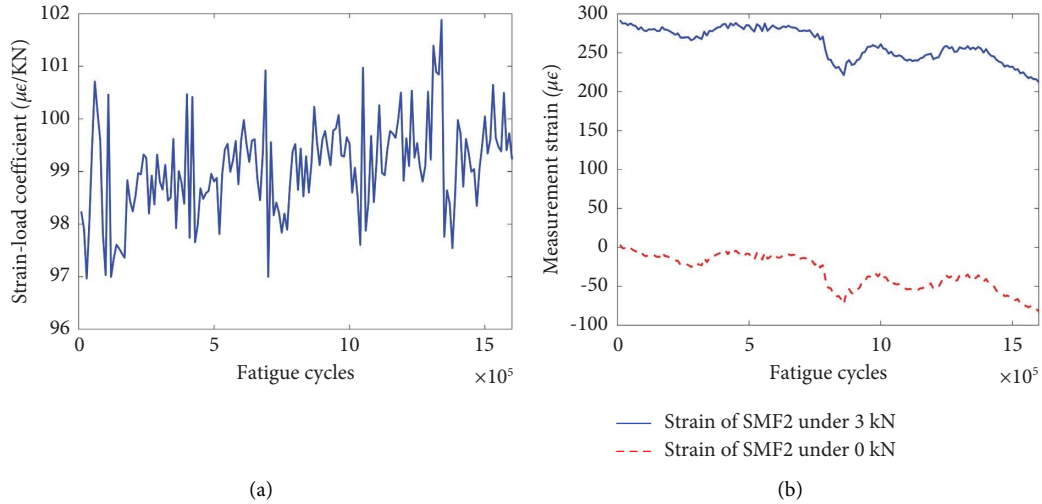
(a)

Strain of SMF2 under 3 kN
Strain of SMF2 under 0 kN

(b)

FIGURE 11: Strain-load coefficient and Gauge2 measurements in fatigue experiment.

(a)

＊ Strain of SMF2 under 3 kN
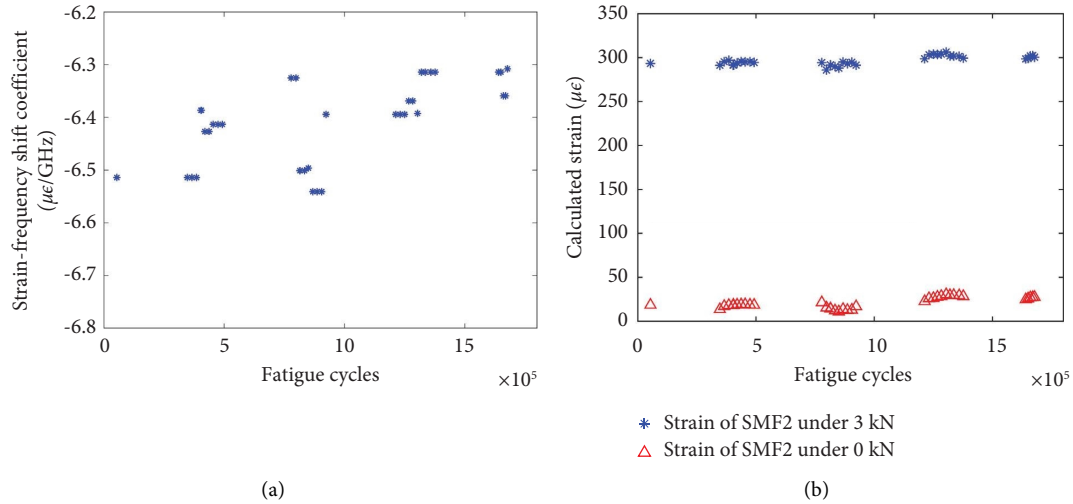△ Strain of SMF2 under 0 kN

(b)

FIGURE 12: Strain-frequency shift coefficient and calculated strain of SMF2 in fatigue experiment.

nonzero values in Figure 12(b) when the tension load is 0 kN. These two diagrams demonstrate that strain measurement errors of the SMF-based distributed sensing under low-frequency vibration load is negligible when a constant strain-frequency shift coefficient is adopted. Although the fatigue experiments do not show a significant influence on the strain-frequency shift coefficient, there is a clear tendency that the proportion of null values in the SMF2 measurements increases with the increase of fatigue cycles. These null values in strain measurements are shown as a white area in Figure 13(a). The proportion of null value with an increase in the fatigue cycle is shown in Figure 13(b).
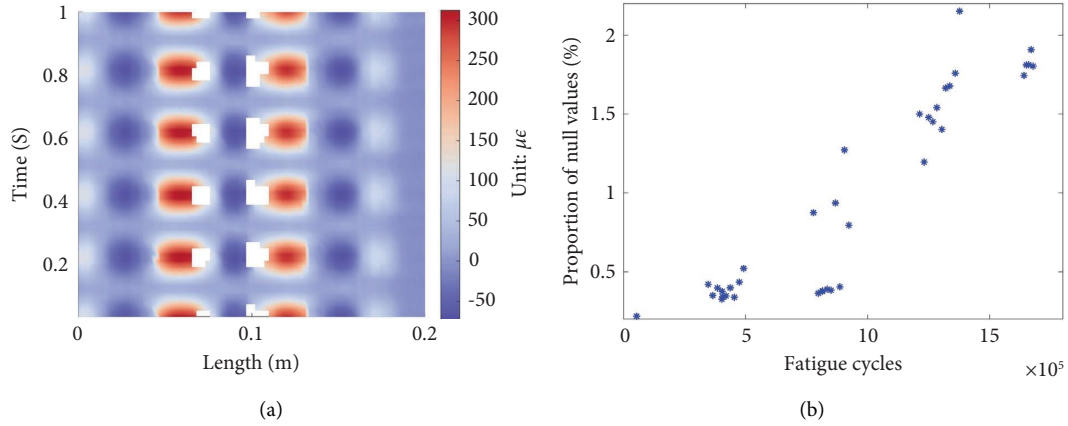
(a)

(b)

FIGURE 13: Null values in measurements of SMF2 in fatigue experiment.

5. Conclusions

This study investigates the robustness of single-mode fibres, as strain sensors, for in-field applications, where operational and environmental conditions such as thermal fluctuations and vibration loads can influence the reliability of the strain distribution. Because SMF does not measure strains directly, there needs to be a conversion coefficient used for transferring the recorded frequency shifts to strain output. This paper investigates the influence of temperature and vibration (fatigue load) on the calculation of this conversion coefficient. To this aim, two experiments were conducted separately on a CFRP specimen under thermal and low-frequency vibration load. The strain measurement was compared with strain gauge readings, and the errors of the SMF-based distributed sensing were investigated by strain-frequency shift coefficient analyses under temperature fluctuations and mechanical vibrations. The conclusions of this work can be summarized as follows:

(i) Temperature fluctuations induce non-negligible errors in strain measurement even with temperature compensation. This error is mainly caused by the mechanical deterioration of adhesives. However, there exists a temperature insensitive range in which this error is negligible. For example, the temperature insensitive range in this study is −20°C to 55°C. Calibration of the strain-frequency shift coefficient is necessary for high accurate strain measurements when the measurement temperature is out of this range for in-field applications.

(ii) SMF-based distributed sensing obtained more strain information compared to strain gauges in both the static loading experiment and fatigue experiment. A reading creep of Gauge2 is observed even though the strain-load coefficient is stable during the entirety of the fatigue experiment. In contrast, the calculated strain and strain-frequency coefficient of SMF2 remained stable during the whole fatigue experiment, which means that strain measurement errors of SMF-based distributed

sensing under low-frequency vibration load is negligible. This conclusion illustrates the advantage of SMF for accurate distributed sensing in low-frequency vibration environments compared to strain gauges.

(iii) Although the fatigue experiments do not show a significant influence on SMF2 measurement values, there is a clear tendency that the number of null values in SMF measurements will increase as the fatigue cycles increase. Therefore, data reconstruction algorithms are required for recovering the strain information when SMF is adopted for strain measurement of composite laminate under low-frequency vibration load. It is worth noting that excessive data reconstruction may lead to the suppression of important features in the strain field, which can have adverse effects on various applications, including damage detection. Specifically, while the primary goal of the smoothing process is to restore the null values arising under low-frequency vibration load, it can also unintentionally dampen critical strain features near the damaged region, thereby hampering potential uses such as damage detection.

Data Availability

The MAT-File data used to support the findings of this study are available from the corresponding author upon request.

Conflicts of Interest

The authors declare that they have no conflicts of interest.

Authors' Contributions

Yingwu Li was involved in conceptualization, software, methodology, visualization, investigation, and writing the original draft. Zahra Sharif-Khodaei was involved in conceptualization, supervision, methodology, resources, writing, reviewing, and editing.

References

[1] X. Zhang, Y. Chen, and J. Hu, "Recent advances in the development of aerospace materials," *Progress in Aerospace Sciences*, vol. 97, pp. 22–34, 2018.

[2] R. Di Sante, "Fibre optic sensors for structural health monitoring of aircraft composite structures: recent advances and applications," *Sensors*, vol. 15, no. 8, Article ID 18666, 2015.

[3] S.-W. Kim, M.-C. Cha, I. Lee, E.-H. Kim, I.-B. Kwon, and T.-K. Hwang, "Damage evaluation and strain monitoring of composite plates using metal-coated FBG sensors under quasi-static indentation," *Composites Part B: Engineering*, vol. 66, pp. 36–45, 2014.

[4] M. Saeedifar and D. Zarouchas, "Damage characterization of laminated composites using acoustic emission: a review," *Composites Part B: Engineering*, vol. 195, Article ID 108039, 2020.

[5] M. Kulpa, T. Howiacki, A. Wiater, T. Siwowski, and R. Sieńko, "Strain and displacement measurement based on distributed fibre optic sensing (DFOS) system integrated with FRP composite sandwich panel," *Measurement*, vol. 175, Article ID 109099, 2021.

[6] B.-H. Choi and I.-B. Kwon, "Damage mapping using strain distribution of an optical fiber embedded in a composite cylinder after low-velocity impacts," *Composites Part B: Engineering*, vol. 173, Article ID 107009, 2019.

[7] J. A. Mills, A. W. Hamilton, D. I. Gillespie et al., "Identifying defects in aerospace composite sandwich panels using high-definition distributed optical fibre sensors," *Sensors*, vol. 20, no. 23, p. 6746, 2020.

[8] R. Soman, J. Wee, and K. Peters, "Optical fiber sensors for ultrasonic structural health monitoring: a review," *Sensors*, vol. 21, no. 21, p. 7345, 2021.

[9] A. Güemes, A. Fernández-López, P. F. Díaz-Maroto, A. Lozano, and J. Sierra-Perez, "Structural health monitoring in composite structures by fiber-optic sensors," *Sensors*, vol. 18, no. 4, p. 1094, 2018.

[10] P. F. Díaz-Maroto, A. Fernández-López, J. García-Alonso, M. Iglesias, and A. Güemes, "Buckling detection of an omega-stiffened aircraft composite panel using distributed fibre optic sensors," *Thin-Walled Structures*, vol. 132, pp. 375–384, 2018.

[11] R. Soman, K. Balasubramaniam, A. Golestani, M. Karpiński, P. Malinowski, and W. Ostachowicz, "Actuator placement optimization for guided waves based structural health monitoring using fibre Bragg grating sensors," *Smart Materials and Structures*, vol. 30, no. 12, Article ID 125011, 2021.

[12] R. Soman, "Multi-objective optimization for joint actuator and sensor placement for guided waves based structural health monitoring using fibre Bragg grating sensors," *Ultrasonics*, vol. 119, Article ID 106605, 2022.

[13] M. Mieloszyk, K. Majewska, and W. Ostachowicz, "Application of embedded fibre Bragg grating sensors for structural health monitoring of complex composite structures for marine applications," *Marine Structures*, vol. 76, Article ID 102903, 2021.

[14] M. Mieloszyk, M. Jurek, K. Majewska, and W. Ostachowicz, "Terahertz time domain spectroscopy and imaging application for analysis of sandwich panel with embedded fibre Bragg grating sensors and piezoelectric transducers," *Optics and Lasers in Engineering*, vol. 134, Article ID 106226, 2020.

[15] D. Saenz-Castillo, M. I. Martín, S. Calvo, and A. Güemes, "Real-time monitoring of thermal history of thermoplastic automatic lamination with FBG sensors and process modelling validation," *Smart Materials and Structures*, vol. 29, no. 11, Article ID 115004, 2020.

[16] V. Buchinger and Z. Sharif Khodaei, "Vacuum assisted resin transfer moulding process monitoring by means of distributed fibre-optic sensors: a numerical and experimental study," *Advanced Composite Materials*, vol. 31, no. 5, pp. 467–484, 2021.

[17] F. Lambinet and Z. Sharif Khodaei, "Development of hybrid piezoelectric-fibre optic composite patch repair solutions," *Sensors*, vol. 21, no. 15, p. 5131, 2021.

[18] S. Goossens, F. Berghmans, Z. Sharif Khodaei et al., "Practicalities of BVID detection on aerospace-grade CFRP materials with optical fibre sensors," *Composite Structures*, vol. 259, Article ID 113243, 2021.

[19] A. Güemes, A. Fernández-López, and B. Soller, "Optical fiber distributed sensing-physical principles and applications," *Structural Health Monitoring*, vol. 9, no. 3, pp. 233–245, 2010.

[20] C. Xu and Z. Sharif Khodaei, "Shape sensing with Rayleigh backscattering fibre optic sensor," *Sensors*, vol. 20, no. 14, p. 4040, 2020.

[21] J. Sierra-Pérez, M. A. Torres-Arredondo, and A. Güemes, "Damage and nonlinearities detection in wind turbine blades based on strain field pattern recognition. FBGs, OBR and strain gauges comparison," *Composite Structures*, vol. 135, pp. 156–166, 2016.

[22] M. Drissi-Habti, V. Raman, A. Khadour, and S. Timorian, "Fiber optic sensor embedment study for multi-parameter strain sensing," *Sensors*, vol. 17, no. 4, p. 667, 2017.

[23] M. Lai, J. Botsis, and J. Cugnoni, "Studies of hygrothermal degradation of a single fiber composite: an iterative approach with embedded optical sensors and numerical analysis," *Composites Part B: Engineering*, vol. 60, pp. 577–585, 2014.

[24] M. Arhant, N. Meek, D. Penumadu, P. Davies, and N. Garg, "Residual strains using integrated continuous fiber optic sensing in thermoplastic composites and structural health monitoring," *Experimental Mechanics*, vol. 58, no. 1, pp. 167–176, 2018.

[25] M. Shamsuddoha, M. David, E. Oromiehie, and B. G. Prusty, "Distributed optical fibre sensor based monitoring of thermoplastic carbon composite cylinders under biaxial loading: experimental and numerical investigations," *Composite Structures*, vol. 261, Article ID 113277, 2021.

[26] S. F. Hassan, S. Kundurthi, S. H. Vattathurvalappil, G. Cloud, and M. Haq, "A hybrid experimental and numerical technique for evaluating residual strains/stresses in bonded lap joints," *Composites Part B: Engineering*, vol. 225, Article ID 109216, 2021.

[27] J. H. L. Grave, M. L. Håheim, and A. T. Echtermeyer, "Measuring changing strain fields in composites with Distributed Fiber-Optic Sensing using the optical backscatter reflectometer," *Composites Part B: Engineering*, vol. 74, pp. 138–146, 2015.

[28] P. Zhu, X. Xie, X. Sun, and M. A. Soto, "Distributed modular temperature-strain sensor based on optical fiber embedded in laminated composites," *Composites Part B: Engineering*, vol. 168, pp. 267–273, 2019.

[29] H. Wang and J.-G. Dai, "Strain transfer analysis of fiber Bragg grating sensor assembled composite structures subjected to thermal loading," *Composites Part B: Engineering*, vol. 162, pp. 303–313, 2019.

[30] J. Etches and G. Fernando, "Evaluation of embedded optical fiber sensors in composites: EFPI sensor response to fatigue loading," *Polymer Composites*, vol. 31, no. 2, pp. 284–291, 2010.

[31] V. Chean, R. Matadi Boumbimba, R. El Abdi, J. Sangleboeuf, P. Casari, and M. Drissi Habti, "Experimental characterization of interfacial adhesion of an optical fiber embedded in a composite material," *International Journal of Adhesion and Adhesives*, vol. 41, pp. 144–151, 2013.

[32] P. Mindermann, M. Gil Pérez, N. Kamimura, J. Knippers, and G. T. Gresser, "Implementation of fiber-optical sensors into coreless filament-wound composite structures," *Composite Structures*, vol. 290, Article ID 115558, 2022.

[33] S. T. Kreger, D. K. Gifford, M. E. Froggatt, B. J. Soller, and M. S. Wolfe, "High resolution distributed strain or temperature measurements in single-andmulti-mode fiber using swept-wavelength interferometry," in *Optical Fiber Sensors*Optica Publishing Group, Washington, DC, USA, 2006.

[34] A. Barrias, J. R. Casas, and S. Villalba, "Distributed optical fibre sensors in concrete structures: performance of bonding adhesives and influence of spatial resolution," *Structural Control and Health Monitoring*, vol. 26, no. 3, Article ID e2310, 2019.

[35] F. Falcetelli, D. Cristiani, N. Yue et al., "Qualification of distributed optical fiber sensors using probability of detection curves for delamination in composite laminates," *Structural Health Monitoring*, Article ID 147592172211411, 2022.

[36] F. Clauß, M. A. Ahrens, and P. Mark, "Thermo-mechanical experiments on reinforced concrete beams: assessing thermal, mechanical, and mixed impacts on fiber optic measurements," *Structural Concrete*, vol. 23, 2022.

[37] Y.-S. Kwon, K. Naeem, M. Y. Jeon, and I.-B. Kwon, "Enhanced sensitivity of distributed-temperature sensor with Al-coated fiber based on OFDR," *Optical Fiber Technology*, vol. 48, pp. 229–234, 2019.

[38] F. Lambinet and Z. Sharif Khodaei, "Measurement platform for structural health monitoring application of large scale structures," *Measurement*, vol. 190, Article ID 110675, 2022.

[39] D. G. Bekas, Z. Sharif-Khodaei, and M. F. Aliabadi, "An innovative diagnostic film for structural health monitoring of metallic and composite structures," *Sensors*, vol. 18, no. 7, p. 2084, 2018.

[40] F. Lambinet and Z. S. Khodaei, "Damage detection & localization on composite patch repair under different environmental effects," *Engineering Research Express*, vol. 2, no. 4, Article ID 045032, 2020.

[41] K. Feng, J. Cui, D. Jiang et al., "Improvement of the strain measurable range of an OFDR based on local similar characteristics of a Rayleigh scattering spectrum," *Optics Letters*, vol. 43, no. 14, pp. 3293–3296, 2018.

[42] S. Zhao, J. Cui, L. Suo, Z. Wu, D.-P. Zhou, and J. Tan, "Performance investigation of OFDR sensing system with a wide strain measurement range," *Journal of Lightwave Technology*, vol. 37, no. 15, pp. 3721–3727, 2019.

[43] M. Gupta, J. Gao, C. C. Aggarwal, and J. Han, "Outlier detection for temporal data: a survey," *IEEE Transactions on Knowledge and Data Engineering*, vol. 26, no. 9, pp. 2250–2267, 2014.

[44] H. Shen, X. Li, Q. Cheng et al., "Missing information reconstruction of remote sensing data: a technical review," *IEEE Geoscience and Remote Sensing Magazine*, vol. 3, no. 3, pp. 61–85, 2015.

[45] D. Stankovic, L. A. Bisby, and G. P. Terrasi, "Influence of temperature on the mechanical performance of unidirectional carbon fiber reinforced polymer straps," *Materials*, vol. 14, no. 8, p. 1903, 2021.

[46] C. Hong, Q. Yang, X. Sun, W. Chen, and K. Han, "A theoretical strain transfer model between optical fiber sensors and monitored substrates," *Geotextiles and Geomembranes*, vol. 49, no. 6, pp. 1539–1549, 2021.